Computers in Biology and Medicine 108 (2019) 288–304

Contents lists available at ScienceDirect

Computers in Biology and Medicine

journal homepage: www.elsevier.com/locate/compbiomed

Smeared multiscale finite element model for electrophysiology and ionic transport in biological tissue

M. Kojic[a,b,c,*], M. Milosevic[b,d], V. Simic[b], V. Geroski[b], A. Ziemys[a], N. Filipovic[e], M. Ferrari[a]

[a] Houston Methodist Research Institute, The Department of Nanomedicine, 6670 Bertner Ave., R7-117, Houston, TX, 77030, USA
[b] Bioengineering Research and Development Center BioIRC Kragujevac, Prvoslava Stojanovica 6, 3400, Kragujevac, Serbia
[c] Serbian Academy of Sciences and Arts, Knez Mihailova 35, 11000, Belgrade, Serbia
[d] Belgrade Metropolitan University, Tadeuša Košćuška 63, 11000, Belgrade, Serbia
[e] University of Kragujevac, Faculty for Engineering Sciences, Sestre Janic 6, 34000, Kragujevac, Serbia

ARTICLE INFO

Keywords:
Electrophysiology
Nerve network
Biological tissue
Cell interior
Organelles
Multiscale models
Composite smeared finite elements

ABSTRACT

Basic functions of living organisms are governed by the nervous system through bidirectional signals transmitted from the brain to neural networks. These signals are similar to electrical waves. In electrophysiology the goal is to study the electrical properties of biological cells and tissues, and the transmission of signals. From a physics perspective, there exists a field of electrical potential within the living body, the nervous system, extracellular space and cells. Electrophysiological problems can be investigated experimentally and also theoretically by developing appropriate mathematical or computational models. Due to the enormous complexity of biological systems, it would be almost impossible to establish a detailed computational model of the electrical field, even for only a single organ (e.g. heart), including the entirety of cells comprising the neural network. In order to make computational models feasible for practical applications, we here introduce the concept of smeared fields, which represents a generalization of the previously formulated multiscale smeared methodology for mass transport in blood vessels, lymph, and tissue. We demonstrate the accuracy of the smeared finite element computational models for the electric field in numerical examples. The electrical field is further coupled with ionic mass transport within tissue composed of interstitial spaces extracellularly and by cytoplasm and organelles intracellularly. The proposed methodology, which couples electrophysiology and molecular ionic transport, is applicable to a variety of biological systems.

1. Introduction

In this study we extend our previously formulated smeared methodology for modeling mass transport in biological tissue to electrophysiological problems and ionic transport. Here, we first briefly outline the motivation for the development of the models applicable in these new areas.

Fundamental processes in living organisms are governed by the nervous system. The physical foundation for the functioning of this system is the generation and propagation of electrical signals. The electrical field in the living organisms includes not only the nervous system – central unit (brain) and network of nerves, but also the entire tissue space: extracellular domain, cell membranes and intracellular space (cytosol and organelles).

The basic approach in determining the electrophysiological properties of all compartments and signal propagation characteristics is in designing experimental procedures and clinical protocols. Here we cite examples of these related mainly to heart electrophysiology. For example, in Ref. [1] a so called 'clamp' experiment was designed to determine characteristics of the membrane currents, with formulation of constitutive relations and material parameters for currents conduction. These relationships established a basis for subsequent experiments, modifications and extension of the constitutive relationships, e.g. Refs. [2–5].

A large number of computational models have been introduced, in analytical and numerical (computational) form. The models are related to electrical signal propagation within neural cells, among cells, along nerve fibers-axons, and within the extracellular space. The models incorporate enormous complexities which include, among many factors, the role of various transmitting molecules, currents carried by ions through membranes and composite media, as well as intricate geometry. The complexity of the material parameters is illustrated in Fig. 1 (a), showing the conductivities of potassium and sodium molecules passing through a cell membrane - in terms of the membrane potential

* Corresponding author. Houston Methodist Research Institute, The Department of Nanomedicine, 6670 Bertner Ave., R7-117, Houston, TX, 77030, USA.
E-mail address: mkojic42@gmail.com (M. Kojic).

https://doi.org/10.1016/j.compbiomed.2019.03.023
Received 29 December 2018; Received in revised form 22 March 2019; Accepted 23 March 2019

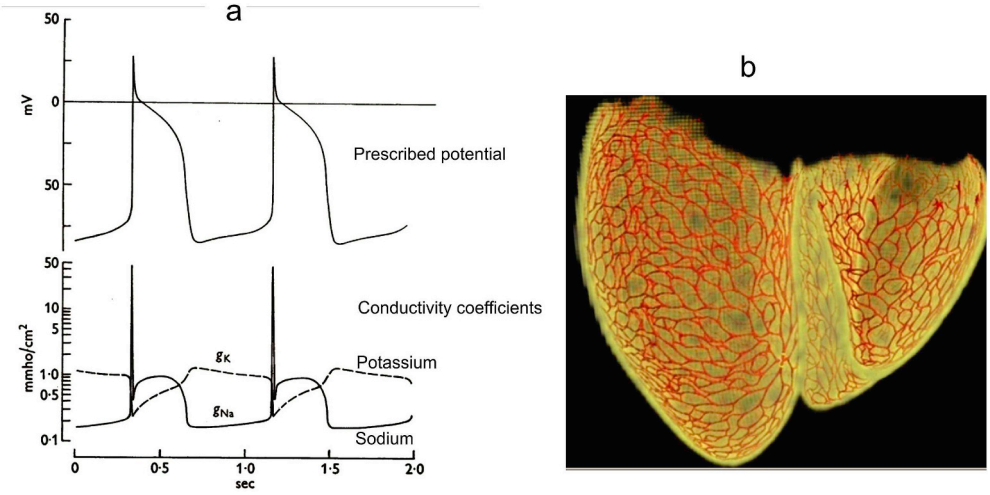

Fig. 1. a) Conduction coefficients for potassium and sodium molecules passing through cell membrane (lower panel) in terms of membrane potential (upper panel), according to Ref. [2]; Purkinje fibers in the heart wall, according to images from Ref. [6].

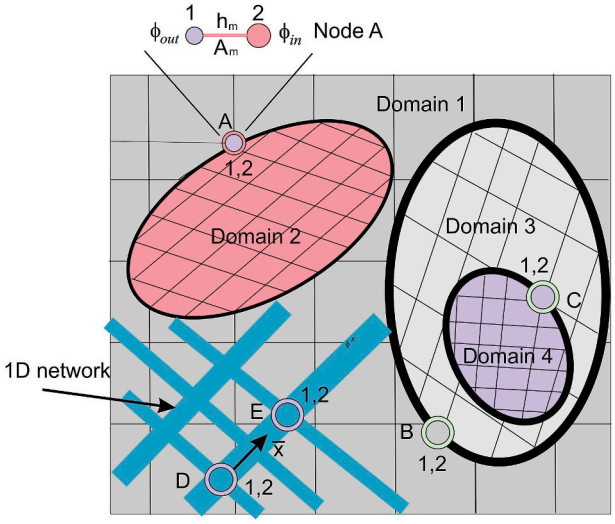

Fig. 2. Schematic of detailed model of a composite medium, 2D representation.

(defined as the difference in potential from inside to outside of the cell) [2]. On the other hand, the network of nerves is very irregular, with irregular branching, as, for example in the case of the Purkinje fibers shown in Fig. 1b [6]. The theoretical foundation for electrical signal transmission in the body can be found in textbooks of general physiology [7–9] or those related to neural physiology [10]. We refer here to few particular computational models related to heart modeling – as a representative organ with electrical signaling coupled to mechanics - and mainly based on the finite element method. A review of computational methods for heart physiology is given in Ref. [11], while those related to coupling electrical field and mechanical response have been the subject of complex modeling in numerous references, for example in Refs. [12–14].

Considering complexity of computational modeling of physical fields (e.g. electrical) within a body, or even within an organ, it is desirable to have a methodology feasible for practical applications. We have introduced a smeared concept for mass transport in capillary system and tissue, refs. [15–18], and demonstrated its superiority with respect to traditional modeling methods. The introduced composite smeared finite element (CSFE) for mass transport served as a basis for generalization in Ref. [19] to finite element (FE) modeling of any gradient-driven field problem. This general formulation will be implemented here to model electrical field within networks of nerves and tissues, and also to couple it with ionic transport.

The variation of electrical potential of cell membranes, due to electrical signals transmitted by the nervous system, triggers other vital processes within living cells. For example, calcium waves within muscle cells, fundamental for the muscle contraction, are induced by changes of the membrane potential. Mechanical models for muscles rely on the calcium concentration changes within cells [12,20–23]. Electrical field also affects transport of charged particles (used in nanotechnology) or drug molecules [24,25] and this kind of mass transport will also be included here.

The paper is organized as follows. In the next section the basic smeared methodology is summarized, while in the next two sections the basic smeared equations are derived for electrical field and ionic transport. Then, in Section 5 we demonstrate accuracy and efficiency of the smeared models, and in Section 6 we give the summary and concluding remarks.

2. Basic equations for a general smeared model of a physical field relying on the gradient driven law

Before formulating the smeared methodology, we consider a 'detailed model' of a composite medium. In Fig. 2 is shown a schematic of a medium composed of continuum domains-compartments and a network of fiber-like 1D domain. Note that the domains can have a hierarchical character (domain 4 is within domain 3 in the figure), as in case of cells with organelles inside. It is assumed that each domain has its own FE mesh of continuum elements, while 1D domains (such as blood vessels, or nerve fibers, or axons) have their own 1D finite elements with the coordinate axes along the elements ($\bar{x}$ axis depicted at one of these fibers).

Additionally, the connectivity elements are introduced to couple the fields between two domains with a common boundary. These elements are located at the nodes common for the two domains, as nodes A, B, …,E shown in the model and enlarged (at the top of the figure). Each of the connectivity elements has two nodes, 1 and 2, with nodal values representing the two domains (ϕ_{out} and ϕ_{in} in the figure). Practically, at a common node at the boundary, two nodes are specified at the same spatial position, with the following characteristics: transport coefficient according the membrane (or wall) material property, cross-section equal to the surface area A_m belonging to that node, and the length h_m equal to the membrane (wall) thickness. It can be seen that the detailed model requires significant effort to generate, and in case of complex medium such as tissue, the model generation would be an impractical or even impossible task. This task would be much more demanding if

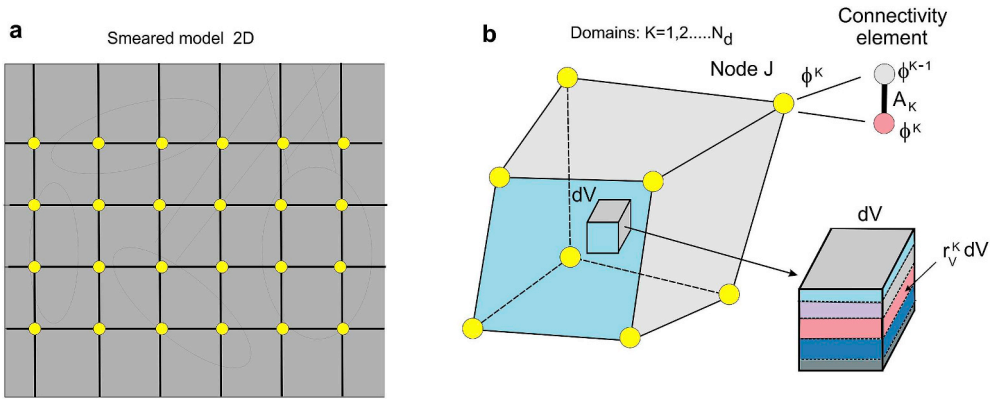

Fig. 3. Schematic of the smeared model. a) Smeared 2D FE mesh for the detailed model in Fig. 2; b) Composite smeared finite element CSFE with different domains and nodal 'degrees of freedom' ϕ^K, and connectivity element at node J between two domains. (from Ref. [19] with permission).

instead of connectivity elements, continuum FEs are employed for membranes.

We now introduce a smeared model by formulating a continuum composite finite element (CSFE) which includes all constituents (continuum and 1D) in a way that the true physical fields, corresponding to a detailed model, are represented in a smeared (a kind of average) sense, with adequate accuracy. A schematic of the smeared model, for the same detailed model of Fig. 2, is shown in Fig. 3a, with only continuum elements present. There are few conceptual steps to formulate the CSFE element.

First, it is necessary to transform the 1D balance equations into the corresponding continuum format. The derivation of the Darcy and diffusion tensors is given in Ref. [18] while, for a general physical field, the continuum transport tensor is derived in Ref. [19]. This tensor can be expressed as

$$D_{ij} = \frac{1}{A_{tot}} \sum_K D_K A_K \ell_{Ki} \ell_{Kj} \tag{1}$$

where

$$A_{tot} = \sum_K A_K \tag{2}$$

is the total area of 1D compartments in a reference volume, surrounding a point in space, with cross-sectional areas A_K; D_K and ℓ_{Ki} are transport coefficients along the 1D elements and directional coefficients, respectively.

The next important statement in the CSFE formulation is that each domain has its own field within the corresponding volume of the CSFE. Hence, the FE node of the CSFE has a number of nodal variables ϕ^K ('degrees of freedom') equal to the number of domains N_d, as shown in Fig. 3b. The domain volume V_K is related to the total element volume as

$$V_K = r_V^K V, \quad \text{and} \quad dV_K = r_V^K dV \tag{3}$$

where r_V^K is the volumetric fraction.

Finally, we include connectivity elements to couple the corresponding domains. Namely, at each node we specify connectivity elements coupling two domains, according to the above described connectivity elements in the detailed model. The cross-sectional area A_{JK} of a connectivity element at node J can be expressed in the form

$$A_{JK} = (r_{AV}^K V_K)_J = (r_{AV}^K r_V^K V_K)_J \tag{4}$$

where r_{AV}^K is the area coefficient, i.e.

$$r_{AV}^K = \frac{A_K}{V_K} \tag{5}$$

and $(V_K)_J$ is the volume of the total space of the continuum belonging to the node J. Note that all the surfaces, volumes and the volumetric and area ratios, are assigned to nodes, which in practical applications is convenient for modeling of any non-homogenous property.

The general form of balance equation of a gradient-driven physical process can be written in the form [26].

$$c_m \frac{\partial \Phi}{\partial t} = D_{ij} \frac{\partial^2 \Phi}{\partial x_i \partial x_j} + q_V, \quad sum\ on\ i, j;\ i, j = 1,2,3 \tag{6}$$

where Φ is physical quantity of the process; c_m is "mass coefficient" ($=0$ for Darcy flow through porous media, $=1$ for diffusion, and $=\rho c_T$ for heat conduction, where ρ is mass density and c_T is specific heat); q_V is the volumetric flux. The finite element balance equations for continuum elements (including the one-dimensional elements represented by the continuum with the corresponding volumetric fraction and transport tensor), for a domain K, time step Δt and equilibrium iteration i, can be written as [19,27].

$$\left(\frac{1}{\Delta t}\mathbf{M} + \mathbf{K}\right)^{(i-1)} \Delta\mathbf{\Phi}^{(i)} = \mathbf{Q}^{ext} + \mathbf{Q}^{v} - \frac{1}{\Delta t}\mathbf{M}^{(i-1)}(\mathbf{\Phi}^{(i-1)} - \mathbf{\Phi}^{t}) - \mathbf{K}^{(i-1)}\mathbf{\Phi}^{(i-1)} \tag{7}$$

where $\mathbf{\Phi}^t$ and $\mathbf{\Phi}$ are nodal variables at the start and end of the time step, $\mathbf{Q}^{ext}$ is the nodal vector due to external effects to the finite element, matrices $\mathbf{M}$ and $\mathbf{K}$, and volumetric nodal vector $\mathbf{Q}^V$, are

$$M_{IJ} = \int_V c_m N_I N_J r \frac{k}{V} dV$$

$$K_{IJ} = \int_V D_{ij} N_{I,i} N_{J,j} r \frac{k}{V} dV, \ \ sum\ on\ i, j:\ i, j = 1,2,3$$

$$Q_I^V = \int_V N_I q_V r_V^K dV$$

where N_I are interpolation functions and V is the element volume. Note that we use the implicit Euler backward integration scheme, indicated by the right upper indices of the matrices, which is unconditionally stable, provides the best accuracy with no error propagation [28,29].

The balance equation for connectivity elements has the form (7), with two nodes, zero volumetric term, and the matrices with the corresponding membrane 'mass' and transport coefficients c_{mm} and D_w.

$$M_{11} = M_{22} = \frac{1}{3} c_{mm} A_m h_m, \quad M_{12} = M_{21} = \frac{1}{6} c_{mm} A_m h_m$$

$$K_{11} = K_{22} = -K_{12} = -K_{21} = D_w A_m$$

The above concept has been implemented to diffusion (including convection) and fluid transport through capillary network and tissue, with demonstration of accuracy of the smeared methodology [15,17,18]. To improve the smeared model accuracy, a correction function was introduced in Ref. [16]. Additional effects present in drug delivery, such as partitioning, can be included in the connectivity elements, as shown in these references. The smeared model can be

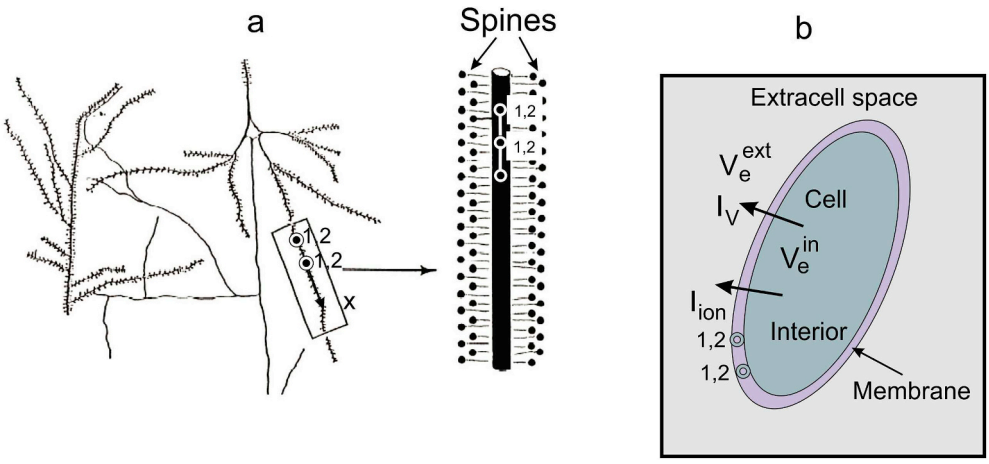

Fig. 4. Schematic of nerve fibers and cells. a) Dendritic tree [3] and 1D finite elements along the fibers with connectivity elements 1,2; b) Cell with current I_V through membrane due to potential difference membrane, and ionic current I_{ion} due to molecule flow modeled by connectivity elements 1,2.

extended to composite media with solid fibers in a way shown in Ref. [30]. Accuracy of the 1D current flow with axial and lateral currents, modeled by a composite 1D finite element, is shown in Appendix 1.

3. Smeared model for electrical field

Here, the fundamental equations for electrostatics are summarized and then the smeared model is formulated in detail, following the general concept in the previous section.

First, consider electrical flow within nerve fibers. As schematically shown in Fig. 4a, the current flows along the axon, but there is also lateral flow through the axon wall due to so called spines [3,7,9,10,31] shown schematically in Fig. 4a. The governing balance equation relies on the so-called cable theory. For the axial current flow along a nerve without lateral flow, the basic relation is

$$I_x = -G_a \frac{\partial V_e}{\partial x} \tag{10}$$

where I_x is the current density along the fiber axis x (as schematically represented in Fig. 4a) G_a is axial conductivity and V_e is electric potential. We will further use term "current" for current density (A/(unit area)). In case of large nerve fibers, there is practically only the axial flow, and the FE model consists of the 1D elements with a standard form (7) of balance equations [18,19].

The lateral flow can be expressed in the form (taking that current going out of the fiber is positive),

$$I_{mem} = G_m(V_e^{in} - V_e^{ext}) + C_m\left(\frac{\partial V_e^{in}}{\partial t} - \frac{\partial V_e^{ext}}{\partial t}\right) + I_{ion} \tag{11}$$

where G_m and C_m are wall conductivity and capacitance, respectively; V_e^{in} and V_e^{ext} are potentials within fiber and in the surrounding; and I_{ion} is ionic current due to flow of various charged molecules through the wall. The lateral flow is modeled by connectivity elements 1,2 at double nodes along fibers and on the cell membranes (Fig. 4).

The balance equations for axial current flow along the fibers are transformed into the continuum format, with the conductivity tensor according to (1), i.e.

$$G_{ij} = \frac{1}{A_{tot}} \sum_K G_{aK} A_K \ell_{Ki} \ell_{Kj} \tag{12}$$

where G_{aK} are axial conductivities of individual fibers. The lateral flow from fibers and flow through cell membranes are modeled by connectivity elements, with balance equations of the form (7) and matrices (analogous to expressions (9)), i. e.

$$M_{11}^e = M_{22}^e = -M_{12}^e = -M_{21}^e = C_m A_{mem}$$

$$K_{11}^e = K_{22}^e = -K_{12}^e = -K_{21}^e = G_m A_{mem}$$

where A_{mem} is the surface area belonging to nodes 1,2, either from a fiber surface or from a cell membrane. This surface is related to the volumetric fraction of the domain according to (4). Additionally, there is a source term in the balance equation due to ionic current I_{ion} for a node J, as

$$Q_{VJ}^e = A_{memJ} I_{ionJ} \tag{14}$$

Regarding the electrical potential within a continuous media, the fundamental continuity equation can be derived for electrostatics from Maxwell's equations [10] as

$$-\varepsilon \frac{\partial}{\partial t}\left(\frac{\partial^2 V_e}{\partial x_i \partial x_i}\right) = G_i \frac{\partial^2 V_e}{\partial x_i \partial x_i} + q_e^V, \quad sum\ on\ i\colon\ i = 1,2,3 \tag{15}$$

where ε is dielectric constant; G_i are conductivities in coordinate directions x_i; and q_e^V is a source term (due to ion flux). This equation can be transformed into the FE format [27] so that the balance equations has the following form

$$\left(\frac{1}{\Delta t} M_{IJ} + K_{IJ}\right) \Delta V_{eJ}^{(i)} = \left(\frac{1}{\Delta t} M_{IJ} + K_{IJ}\right) V_{eJ}^{(i-1)} + Q_{eI}^V + Q_{eI}^{ext} \tag{16}$$

where Q_{eI}^{ext} are external effects to the element, and

$$M_{IJ} = \varepsilon \int_V \frac{\partial N_I}{\partial x_i} \frac{\partial N_J}{\partial x_i} r_V \, dV, \quad K_{IJ} = G_i \int_V \frac{\partial N_I}{\partial x_i} \frac{\partial N_J}{\partial x_i} r_V \, dV, \ sum\ on\ i\colon\ i = 1,2,3$$

$$Q_{eI}^V = \int_V N_I q_e^V r_V \, dV$$

In case of the continuity domain representing a network of small nerve fibers, we have:

$$M_{IJ} = 0, \quad K_{IJ} = \int_V G_{ij} \frac{\partial N_I}{\partial x_i} \frac{\partial N_J}{\partial x_j} r_V \, dV, \ sum\ on\ i, j\colon\ i, j = 1,2,3 \tag{18}$$

In summary, the main characteristics of the composite smeared finite element (and the corresponding FE model) for electrical potential within a biological system are as follows:

- Large nerve fibers (big axons) are modeled by 1D finite elements, connected to a network of small fibers
- Small fiber network is represented by a continuum with the corresponding volumetric fraction and conductivity tensor (12); the balance equation is (16) with the element matrices (18)
- Continuum domains include: extracellular space, different groups of cells, and organelles within cells. They occupy the volumetric fractions r_V-s of the element, and the balance equation (16) include

matrices and source term (17)
- Lateral current flow from fibers and through membranes of cells and organelles is modeled by 1D connectivity elements with matrices (13) and source terms (14)

The data necessary for the smeared model consists of the geometrical part associated with the FE nodes: volumetric fractions r_V^J, area coefficients r_{AV}^J, volumes V^J belonging to nodes, wall or membrane thicknesses, geometric characteristics of the fiber network; and material data, which also can be associated with the FE nodes: conductivities - within fibers, through membranes and within continuum domains, dielectric constants, capacitances of walls and membranes, characteristics of the ionic currents through membranes.

4. Smeared model for ionic transport

Gradient driven transport of charged molecules (ions)/particles in a continuum space or through biological membranes is affected by the field of electrical potential. Also, the ions change the field of electrical potential, therefore there exists a coupling between ion transport and concentration, and the electrical field. Here, we first summarize the fundamental equations in this physical problem and then present a smeared FE methodology for computational modeling.

The mass flux J_i in direction x_i of ions m has a part corresponding to diffusion and, additionally, a part due to the electrical force based on the Nenrst-Plank equation; and can be expressed as [24].

$$J_i^m = -D\frac{\partial c^m}{\partial x_i} - \frac{Dz^mF}{RT}c^m\frac{\partial V_e}{\partial x_i} \tag{19}$$

where D is diffusion coefficient, z^m is molecule valence, F is the Faraday constant, T is absolute temperature, and c^m is concentration. Then the mass balance equation is

$$\frac{\partial c^m}{\partial t} = \frac{\partial}{\partial x_i}\left[D\frac{\partial c^m}{\partial x_i} + \frac{Dz^mF}{RT}c^m\frac{\partial V_e}{\partial x_i}\right], \quad sum\ on\ i\text{:}\ \ i = 1,2,3 \tag{20}$$

The FE balance equation which follows from this equation has the form (7) for the concentration field, with the source term due to electrical effects

$$Q_I^{mE} = \frac{DFz^m}{RT}\int_V N_I\frac{\partial}{\partial x_i}\left(c^m\frac{\partial V_e}{\partial x_i}\right)r_V^K dV \tag{21}$$

This source term can be evaluated as follows:

$$Q_I^{mE} = Q_I^{mE1} + Q_I^{mE2} \tag{22}$$

where

$$Q_I^{mE1} = \frac{DFz^m}{RT}\int_V N_I\frac{\partial c^m}{\partial x_i}\frac{\partial V_e}{\partial x_i}dV \tag{23}$$

$$Q_I^{mE2} = \frac{DFz^m}{RT}\int_V N_I c^m\frac{\partial^2 V_e}{\partial x_i\partial x_i}dV = -\frac{1}{\varepsilon}\frac{DF^2z^m}{RT}\int_V N_I c^m\left(\sum_m z^m c^m\right)dV \tag{24}$$

In the last equation the electrostatic balance of charge due to ionic charge contribution is considered, according to Ref. [24]. Summation in the last equation includes all ion types involved in mass transport.

The source term in equation (17) due to presence of ions within the domain can be calculated as

$$q_e^V = \sum_m z_m F\frac{\partial c_m}{\partial t} \tag{25}$$

Next, we present the fundamental relations for ionic transport through cell membranes, following refs. [25,32]. The relations given below are based on the Nernst equation

$$\frac{a_i}{a_o} = e^{-N}, \quad N = \frac{zFE}{RT} \tag{26}$$

where a_i and a_o are molecular activities on the two sides of the membrane ('inside' and 'outside'). Assuming linear distribution of the gradient of electrical potential across the membrane thickness, the flux through the membrane can be expressed as

$$J = J_n + J_d = P_n(a_{on} - a_{in}) + P_d\frac{N}{e^N - 1}(a_{od} - a_{id}e^N) \tag{27}$$

where indices 'n' and 'd' stay for neutral and ionized forms of molecules for fluxes J_n and J_d, permeability coefficients P_n and P_d, and molecular activities. The steady state of the electrical field is assumed. Activations can be related to the concentration of molecules c as

$$a_n = f_n c, \quad a_d = f_n k_{pH} c \tag{28}$$

where f_n and k_{pH} are material constants which take into account chemical and electrochemical characteristics of the transported molecules (details are given in Refs. [25,32]). Substituting (28) into (27) and using material properties at both membrane sides, the expression for the molecular flux can be expressed as

$$J = P_n f_n(c_o - c_i) + P_d\frac{N}{e^N - 1}f_n(k_{pH}^o c_o - e^N k_{pH}^i c_i) \tag{29}$$

where k_{pH}^o and k_{pH}^i are constants at the two sides of the membrane.

The relation (29) leads to formulation of the diffusion matrix for the membrane connectivity element. The matrix terms in equation (9) are now

$$K_{11} = -K_{21} = A_{mem}\left(P_n f_n + P_d\frac{N}{e^N - 1}f_n k_{pH}^0\right)\cdot K_{22} = -K_{12} = A_{mem}\left(P_n f_n + P_d\frac{Ne^N}{e^N - 1}f_n k_{pH}^i\right) \tag{30}$$

where A_{mem} is the membrane surface belonging to a FE node, according to eq. (4). In one of the examples (Example 5.3) we will demonstrate implementation of this connectivity element.

We note that the composite smeared finite element contains field of concentration of each ion and for each domain. A practical computational procedure in modeling the coupled problem between electrical field and ionic concentration is implemented in our FE software package PAK [33] with the following steps:

1) Electric potential field is determined using concentration distribution from the end of previous step, for all ion types.
2) Concentration field of each molecule is calculated using the electrical potential from step 1.

Steps 1 and 2 are repeated until differences in solutions for both electrical potential and concentration of ions satisfy the adopted convergence criteria.

5. Discussion – reference to other computational models

In this section we compare the introduced smeared model with other computational models available in literature. Electrophysiology, as well as particulate/molecular transport, has long been the subject of experimental and theoretical research. Various numerical models, starting with analytical to today's modern computational models, have been formulated and implemented. Here we refer mainly to the models related to heart electrophysiology and emphasize novel features of our smeared models important for applications.

Initial models of cardiac electrophysiology rely on the seminal work of Hodgkin and Huxley [1]. In reviews [11,34] monodomain and bidomain models of tissue, connected to the basic cell models, are presented for heart electrophysiology. A critical analysis regarding practical applications of these models is given in Ref. [35], with particular reference to the format of data preparation, as CellML and software

simulator Chaste [36]. The approach that most resembles our smeared models in principle, is the so-called bidomain model introduced decades ago [37–40], derived from discrete models by using homogenization procedures. The bidomain model was further extended to a model with two types of cells, called the extended bidomain model [41]. The governing balance equations of the three continuum domains (extracellular space and two cell types) in Ref. [41] are derived according to the ohmic conduction law using the conductivity/resistance characteristics of each domain. Additionally, the terms corresponding to membrane conduction and ionic currents I_{ion} between the three domains are included. These membrane terms take into account the membrane conduction and capacitance properties, and the corresponding area-to-volume ratios. The FE nodal variables consist of the potentials of the three continuum domains.

For purposes of comparison to our model, we show here the fundamental equations of reference [41] using our notation. For the three domains, cell group 1, cell group 2, and extracellular space, the equations are (terms not important for our analysis: stimulus current and gap effects, are omitted).

$$-r_{AV}^{(1)}\frac{\partial}{\partial x_i}\left[C_m^{(1)}\left(\frac{\partial V_e^{(1)}}{\partial t}-\frac{\partial V_e^{(ext)}}{\partial t}\right)+I_{ion}^{(1)}\right]+\frac{\partial}{\partial x_i}\left(G^{(1)}\frac{\partial V_e^{(1)}}{\partial x_i}\right)=0$$

$$-r_{AV}^{(2)}\frac{\partial}{\partial x_i}\left[C_m^{(2)}\left(\frac{\partial V_e^{(2)}}{\partial t}-\frac{\partial V_e^{(ext)}}{\partial t}\right)+I_{ion}^{(2)}\right]+\frac{\partial}{\partial x_i}\left(G^{(2)}\frac{\partial V_e^{(2)}}{\partial x_i}\right)=0$$

$$\frac{\partial}{\partial x_i}\left(G^{(1)}\frac{\partial V_e^{(1)}}{\partial x_i}\right)+\frac{\partial}{\partial x_i}\left(G^{(2)}\frac{\partial V_e^{(2)}}{\partial x_i}\right)+\frac{\partial}{\partial x_i}\left(G^{(ext)}\frac{\partial V_e^{(ext)}}{\partial x_i}\right)=0$$

where the upper indices 1 and 2 correspond to the first and second group of cells, while 'ext' stands for the extracellular space. These equations are then transformed to the FE format in a standard Galerkin weighting procedure used above [26], and integration is performed over the entire domain volume.

We further summarize differences between our smeared model and the bidomain or the extended bidomain model (called further as the previous models). Also, we emphasize our new formulations.

1. Considering electrophysiology, the first and fundamental difference between previous models and our smeared models is that the previous models are case sensitive, while ours are general. The previous models rely on the apparent material properties of the entire tissue, while our models use the true material parameters, independent on the tissue composition. This difference comes from the assumptions used in the derivation of the governing balance equations. In the previous models, these equations (e.g. equation (31)) are derived by homogenization over the entire tissue volume, including cell membranes, through the area factor r_{AV} and continuity conditions at the membranes [40]. Integration is therefore performed over the entire domain, without including the participation of volumetric fractions of the individual constituents (compartments). This represents a significant drawback which can be illustrated in the following simplified example: Assume we have a current flow to a closed domain composed of different types of cells and extracellular space, separated by membranes, with their own conductivities and dielectric constants. The electric charge and potential within each of the constituents must depend on their respective volumetric fractions. Therefore, the traditional models practically deal with the apparent material parameters which depend on the structural composition of the tissue. On the other hand, our smeared models consider the entire medium as a composite where a compartment K occupies the volume specified by volumetric fraction r_V^K, and the balance equations are set by using the true material parameters of that compartment. No additional condition is employed and the equations are independent of the tissue composition. The compartments considered here include: large vessels, large neural fibers, capillary network, small neural fibers, extracellular space, and different groups of cells composed of cytosol and organelles. The spatial numerical integration goes over the $r_V^K V$ occupied by the compartment K. For organelles, both in diffusion and in electrophysiology, the volume fraction has a hierarchical character, i. e. for a cell group N,

$$V_N^k = r_V^k r_V^N V \tag{32}$$

where r_N^k is the relative volume ratio of the organelle with respect to the cell volume, whose ratio r_V^N is related to the finite element volume V. Accuracy of our smeared models is assessed by comparison to the detailed FE models of a composite tissue, given here and in our previous publications [15,16,18,42].

2. A significant novelty of the smeared model is the representation of a 1D processes (e.g. fluid flow, diffusion, electric conduction within a fiber-like domains) by continuum equations with a consistent transport tensor (1); and integration goes over the CSFE volume occupied by the 1D network space. This approach was initially introduced in our cited references for convective and diffusive transport, along with the demonstration of the accuracy of solutions, and herein is applied to electrophysiology. The entire His-Purkinje system of the heart [43] can be modeled using our smeared continuum representation in a way analogous to modeling a capillary network [18]. Our model has a significant distinction with respect to, for example, the model in Ref. [44] which is based on the bidomain formulation and averaging over the fiber cross section.
3. The electrostatic equation (15) used in our formulation are more general than those in (31), since they take into account the rate of change of the potential (the term on the left-hand side), which previous models omit.
4. Formulation of the connectivity elements between different physical fields is a unique feature of the smeared models. These elements are particularly suitable for including specificities of the membranes (cells, organelles) and vessel walls such as partitioning at the membrane/wall common surface with the continuum, or material nonlinearities in case of transport or electric conduction. The inclusion of gap junctions between cells, introduced in Refs. [41,45], or the condition that connections between Purkinje fibers and tissue occurs at the fiber ends, is straightforward by employing the appropriate connectivity elements. Also, ionic currents due to ion flow through membrane channels (I_{ion}) [5] can be included in these elements, as well as transport of specific molecules such as calcium [46–49]. Geometrical terms related to the connectivity elements are described above (equations (3)–(5)). There are also important features of the connectivity elements regarding the convergence rate during equilibrium iterations at the global level – the matrices of these elements have a so-called tangent character for improved convergence [29]. These elements are also computationally efficient, since they do not require numerical integration (as needed in implementation of equation (31) in traditional models).
5. A 1D finite element is introduced to model current flow which includes current conduction along a neural fiber and lateral loss of electrical charge through the fiber surface [3]. The FE formulation is based on cable theory and the element accuracy is assessed by comparison to analytical solutions; details provided in Appendix 1. This element is formulated for modeling electrical signal transmission along large axons, however it is also applicable for modeling smaller neural fibers such as in case of Purkinje network within the heart. Our concept is straightforward and simple (with demonstrated accuracy) when compared to Ref. [44], where a complex homogenization procedure was employed to couple 1D signal propagation within the Purkinje network to a bidomain continuum model of the heart tissue.
6. Another novelty introduced is our procedure for bidirectional coupling of the ionic transport and electrical field. In the continuous

domains (extracellular space, cell interior, organelles) this procedure relies on equation (20) which is transformed to the FE framework. Also, the coupling is included into our connectivity elements, following formulation given in Ref. [25]. The presented methodology is suitable and straightforward for general applications at the organ level (in Refs. [25,50] only cell interior is considered), as demonstrated by the presented examples.

There are a number of issues, not mentioned above, that are important when considering electrophysiology and coupling to other physical fields in living organisms, for which the smeared methodology can be effectively applied. For example, procedures that improve computational efficiency of the monodomain and bidomain models, e.g. in Refs. [51–54] - with specific solution algorithms [22,55–59], or analysis of stochasticity in the heart electric signal propagation dynamics [60], can be implemented into our smeared models. Finally, coupling electrophysiology to the mechanics of muscles [21,22,61–63], including multiscale muscle models [64], can be efficiently implemented into our smeared models.

Since there are many computational models in electrophysiology and muscle mechanics, particularly related to the heart, validation becomes crucial [65] for patient-specific reliable computer simulations [66].

6. Numerical examples

Several examples are selected. The purpose of these examples is to demonstrate applicability, accuracy and efficiency of the presented smeared modeling methodology. The basic idea is to show accuracy considering electrical signal transfer from nerve fibers to extracellular space and further to cells. The connection between nerve fibers and cells in the model goes via extracellular space which also represents the fiber-cell junctions present in the biological systems. The first example is designed with an electrical gradient across the field. Other examples assume a small isolated region of tissue (here we used the geometry of cells as in Ref. [17]) with prescribed potentials within nerves. Isolated tissue domain means that gradients with respect to the surrounding domain are neglected. The last example includes ionic transport coupled with the field of electrical potential.

6.1. A tissue domain with electrical potential gradient

A square tissue domain is shown in Fig. 5. It is assumed that there is a nerve fiber network, with given constant potential at two boundaries, while the lateral boundaries are impermeable both for tissue and fibers. The data used in the model are

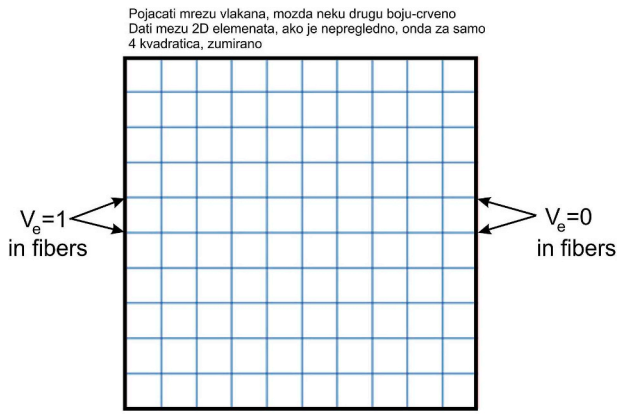

Fig. 5. A square tissue domain (10 × 10 mm) with network of nerves (in red) connected with tissue. Prescribed constant electrical potential at the two boundaries.

Fiber diameter: 0.25 mm Volume fraction: $r_V = 0.35$ (35%)
Membrane conductivity: 0.1 S/mm^2 Capacitance: 0.1 F/mm^2.
Conductivity: Fibers 1 S/mm Tissue: 2 S/mm.
Dielectric constant: 0.1 F/mm.

In Fig. 6 are shown mean potentials developed over time for the tissue and for the fiber domain, obtained by using the detailed model (1D elements for fibers, 2D elements for tissue, and connectivity elements for fiber lateral currents) and the corresponding smeared model (number of potentials at FE nodes is 2 - for fiber and tissue domain). There are some differences, as expected, due to gradients in both fiber and tissue domains. As will be seen in the subsequent examples, this difference is smaller when there is no gradient within fibers (which is physiologically more realistic). Also, the goal of the examples here is to demonstrate accuracy of transport from capillary system to cells or signal propagation from nerve network to cells. Effects of the gradients as in this example are dependent on the model size, which here are not further investigated; accuracy analysis in case diffusion and presence of gradients is given in Ref. [18].

6.2. A tissue domain with cells and organelles

Here, we consider an isolated 2D tissue domain with two groups of cells and with three organelles within each group (as used in Ref. [17]), shown in Fig. 7. Cells have different material parameters and volumetric fractions. It is assumed that six nerve fibers are present (normal to the 2D space), with prescribed potentials as function of time. Three cases of prescribed potential are used – constant, bolus, and as in Purkinje fibers in heart.

Geometry			
Nerve fibers (6)	Mean diameter 4.76	Volumetric fraction 0.043	
Cell group 1 (24)	6.30	0.307	
Organelle 1	3.64	0.334	
Organelle 2	1.16	0.334	
Organelle 3	1.10	0.031	
Cell group 2 (21)	6.16	0.260	
Organelle 1	3.17	0.270	
Organelle 2	1.39	0.051	
Organelle 3	1.46	0.057	
Material data			
Extracell and fibers	Conductivity 10^{-7}	Membrane conductivity 4 10^{-12}	Capacitance 10^{-14}
Cell 1 and organelles	10^{-7}	4 10^{-10}	10^{-12}
Cell 1 and organelles	10^{-7}	4 10^{-12}	10^{-14}
Initial values: E = 0 in extracellular space, 0.07 in cells, 0.05 in organelles			

The detailed model consists of 2D elements used for all continuum domains and also for all membranes of cells and organelles, with prescribed potential at the surfaces of the nerve fibers. In the smeared model we have 2D elements only, which include nerve fibers, all continuum domains and membranes, with 10 nodal potentials as nodal variables (depicted in Fig. 7). Note that all membranes and the surface of the fibers are modeled by connectivity elements (with no additional nodal variables). For the insight into difference in model size of the two models we give the number of equations of the system to be solved: 69457 for detailed model, 1089 for smeared model. Besides the enormous difference in effort to prepare two models, the size of the models and therefore the computational difference is of the order of 10^2.

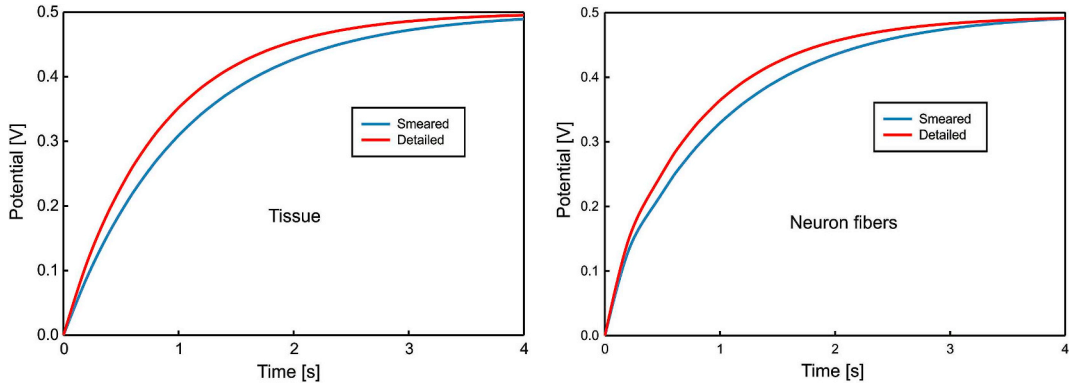

Fig. 6. Mean potential in nerve fibers (left panel) and in tissue (right panel) evolution over time. Prescribed potential in fibers at boundary (Fig. 5).

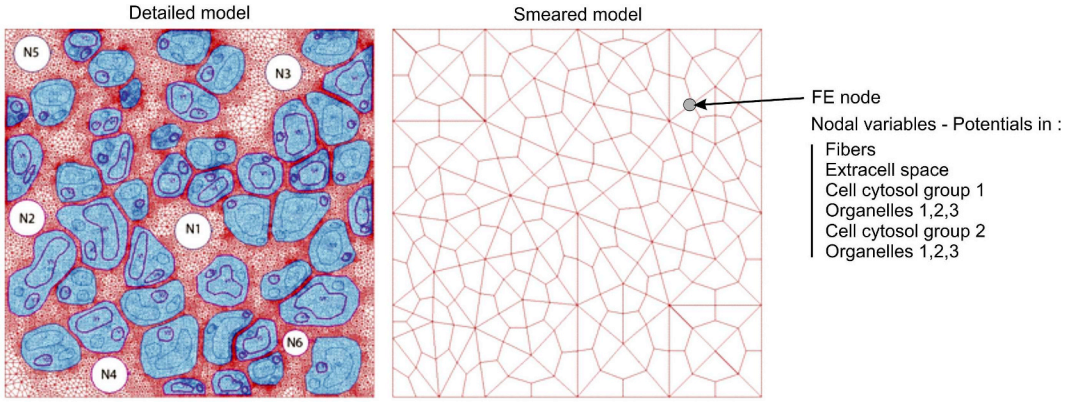

Fig. 7. A tissue domain of size (50 × 50 μm) with cells and nerve fibers (N1 to N6) normal to the plane. Detailed model with 2D elements (left panel) and smeared model (right panel). The data used in the models are given below (units: length μm, potential V, conductivity S/μm, membrane conductivity S/μm2, capacitance F/μm2).

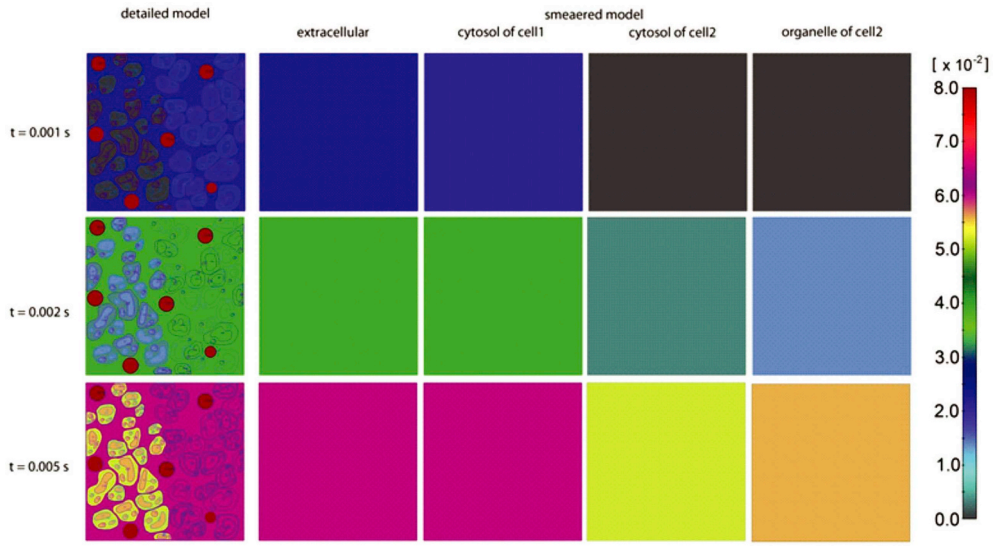

Fig. 8. Fields of electrical potential in case of constant potential of 0.08V within nerve fibers. Three time points and several domains, detailed and smeared model.

6.2.1. Constant potential in fibers

It is assumed that the potential within fibers is constant and equals to 0.08V. We use a small value for prescribed potential in order to detect differences in domains with micron size. The potential fields for three different time points, for detailed and smeared model, are shown in Fig. 8.

It can be seen that the uniform fields of the smeared model agree with the corresponding domains within the detailed model. The evolution of the mean potential for several domains is shown in Fig. 9, demonstrating very high degree of agreement. This is expected since the potential fields in the detailed model are practically uniform for each spatial domain. Some delay can be noticed in potential evolution

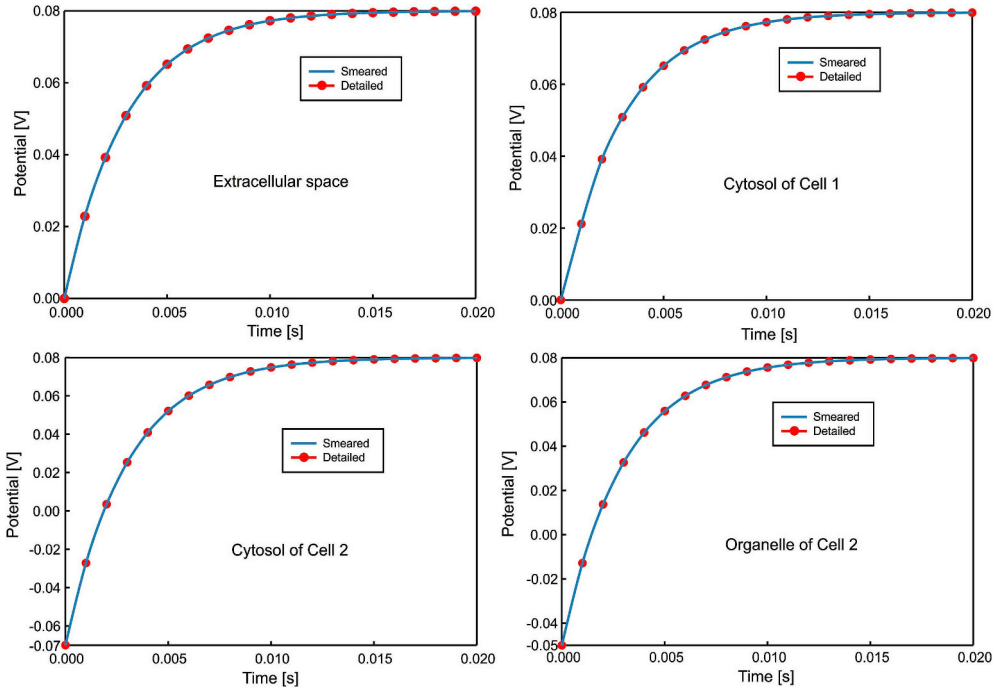

Fig. 9. Evolution of the mean potential in case of constant potential of 0.08V within nerve fibers. Four domains, detailed and smeared model.

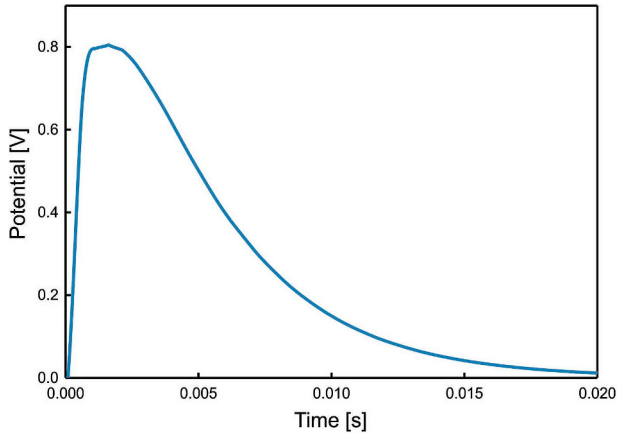

Fig. 10. A bolus-type prescribed electric potential in nerve fibers.

within cells, and particularly within organelles in the cell group 2 due to smaller membrane conductivity for this organelle.

6.2.2. A bolus function for potential in fibers

It is assumed that a bolus-type function is given within nerve fibers, as shown in Fig. 10.

The evolutions of the potential within different domains computed by either model are practically the same, Fig. 11. As in the case of constant potential, there is a small time delay and difference from the prescribed potential within nerve fibers, due to membrane resistances.

6.2.3. A function as in Purkinje fibers

Finally, here we use the function for prescribed potential as in the Purkinje fibers of the heart [2]. Due to the high value of the potential within the fibers, the potentials in all domains are practically as in the fibers, and are the same when using either one of the two models. The evolution of the potential in any of the domains is as shown in Fig. 12.

6.2.4. Model with potassium and sodium currents included

Here we include into the model currents through cell membranes due to potassium and sodium flow through the membranes (in eq. (11)). Details of the calculation of these currents are given in the Appendix 2. We use values of potential corresponding to the last equilibrium iteration, hence it is an Euler backward integration scheme; effects of the integration algorithm of the ionic currents on the solution accuracy is studied in Ref. [67]. It is assumed that the potential in nerve fibers is constant and equal to 0.08V.

Electrical potential field for four time points and for the detailed model is shown in the first row of Fig. 13. It can be seen that the potentials in the interior of cells are different in the two groups due to different material properties. In the second row we display the potential field for cell interior of group 2. It can be seen that there is agreement between the two models.

Graphs for the change of the mean potentials over time within different domains are shown in Fig. 14. The effect of ionic currents can be noted – the ultimate values of potentials are: 0.6V for extracellular space, 0.08V for cells (as is prescribed in fibers). The potential within extracellular space is higher than in cells due to outward net ionic current flow.

6.3. Model with coupled diffusion of ions and electrical flow

In this final example, we consider coupled electrical and concentration fields. The same model as in Fig. 7, but now additionally with five capillaries C1…C5, is shown in Fig. 15. Nodal variables include concentrations in all domains except in nerve fibers, while the potential field is present in all domains except in capillaries. Here, a structural mesh is used for the smeared model to demonstrate that this simple mesh can also provide accurate results. Number of equations for

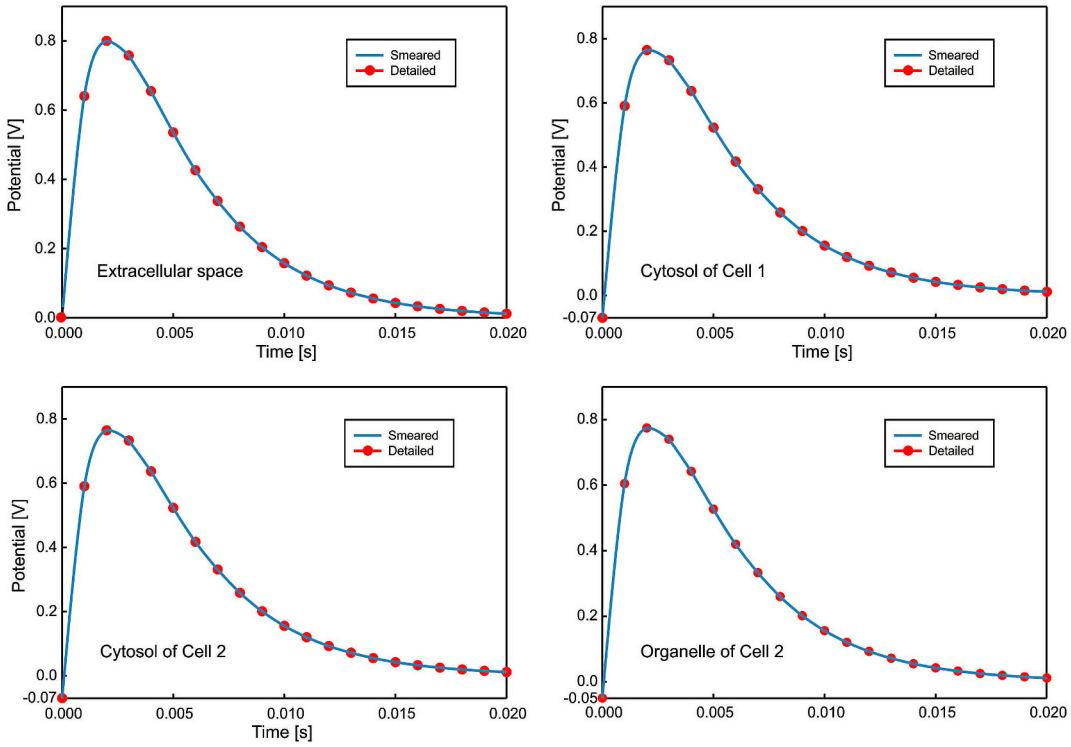

Fig. 11. Electric potential vs. time for detailed and smeared model within different domains for bolus function in Fig. 9 within fibers.

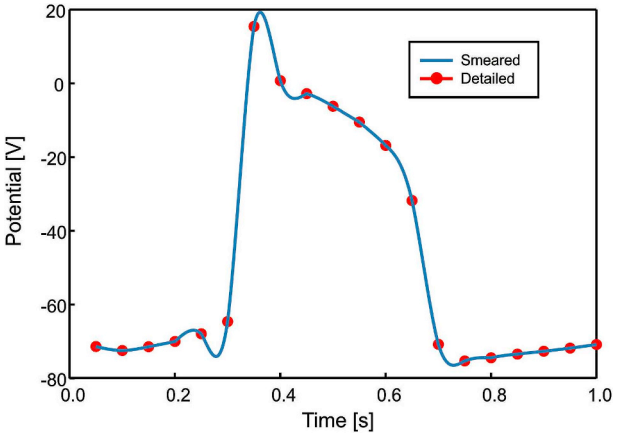

Fig. 12. Electrical waveform within Purkinje fibers of the heart [2].

detailed model is 72458 and for smeared model is 1200.

The same data as for example 6.2 is used for the electrical field, while for diffusion the material data are as follows, according to Ref. [25]: Diffusion coefficient is the same for all continuum domains: 10^3 μm^2/s.

Diffusion coefficients for membranes are also the same for all continuum domains: 10^3 μm/s, Partitioning coefficients: P = 10 at cell membrane of cell group 2, and P = 10 at organelle membrane of cell group 2.

Coefficients P_n, P_d, k_{pH}^o , k_{pH}^i and f_n are equal for all cells and organelles: $P_n = P_d = 1, k_{pH}^o = k_{pH}^i = 10^{-6}, f_n = 1.2382$. Material data for evaluation of the coefficient f_n are as given in Ref. [25].

Bolus-type function is used as in Fig. 10 for both electrical potential (maximum is 0.8 V) within nerve fibers and for concentration in capillaries (maximum is 10^{-4} mg/μm^3).

Concentration and electrical potential field, obtained by the detailed model, at time 1s, is shown in Fig. 16. Differences in concentration

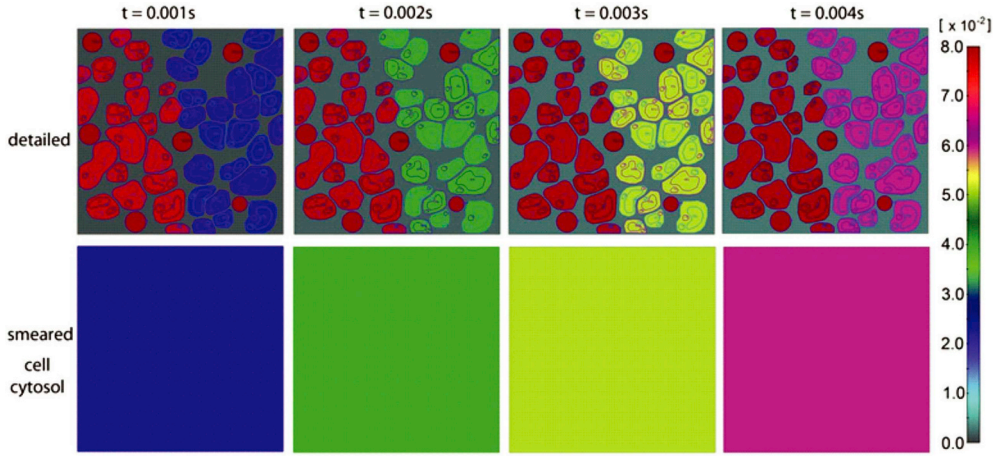

Fig. 13. Fields of electrical potential in case of ionic currents of potassium and sodium included; detailed model – upper panel, smeared model –lower panel.

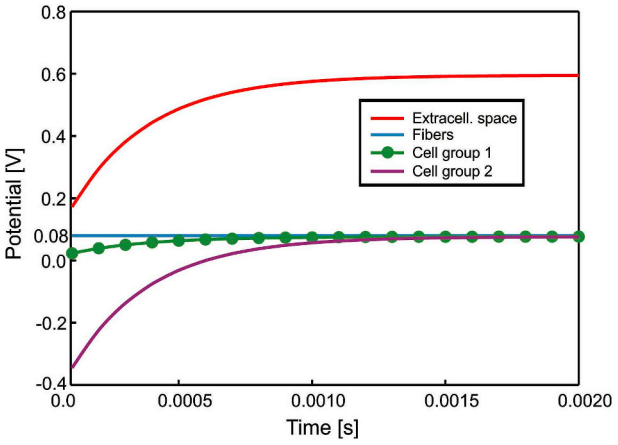

Fig. 14. Evolution of the mean potential in extracellular space and cells, detailed and smeared solutions; with ionic currents of potassium and sodium included.

between the two groups of cells are notable due to partitioning P = 10 for cell group 2. Mean concentration and electrical field evolution, obtained by the two models, are shown in Figs. 17 and 18, respectively. It can be seen, as in previous examples, that there is good agreement between the two models. Some differences are expected due to very non-uniform concentration and electrical potential fields. We have specified some extreme conditions within the model: two cell groups are located in separate spatial domains and with different material properties – it is taken that there is partitioning for cell and organelle membranes of cell group 2.

7. Summary and concluding remarks

A general smeared methodology for field problems, formulated in Ref. [19] as a generalization of the previously published applications for diffusion within tissue [15,17], is extended to include the electrical potential field. This expanding model also incorporates membrane ionic transport, particularly important in muscle and heart electromechanics [1,2,9,21,22]. The concept is further enhanced by including ionic transport in tissue so that the concentration and electrical potential fields are coupled. Also, a composite cable finite element (CCFE) is introduced for electrical signal propagation within axons and its accuracy is verified (see Appendix 1).

Selected examples demonstrate accuracy and efficiency of the smeared method. The composite smeared finite element (CSFE) is a continuum element which contains all domains within the biological system. The domains occupy a volumetric fraction of the element and have their own physical fields, hence the nodal variables include all fields. Moreover, the complex 1-D gradient driven fields are substituted by a continuum representation with the corresponding transport tensor. The physical fields of the CSFE are coupled by connectivity elements

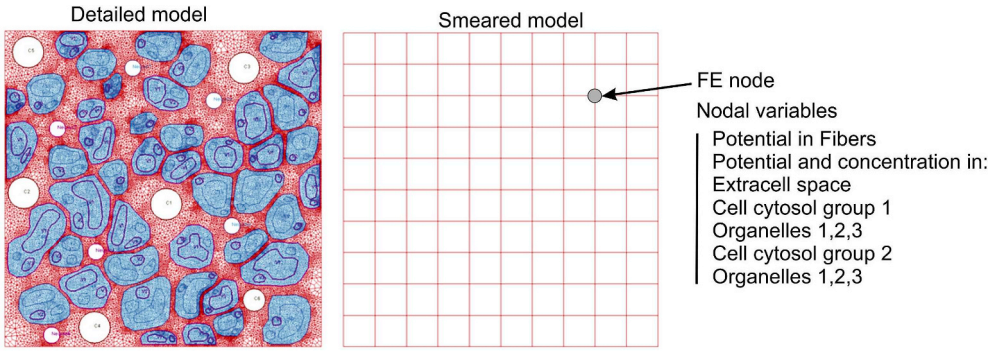

Fig. 15. Detailed and smeared model for coupled electrical flow and ionic diffusion.

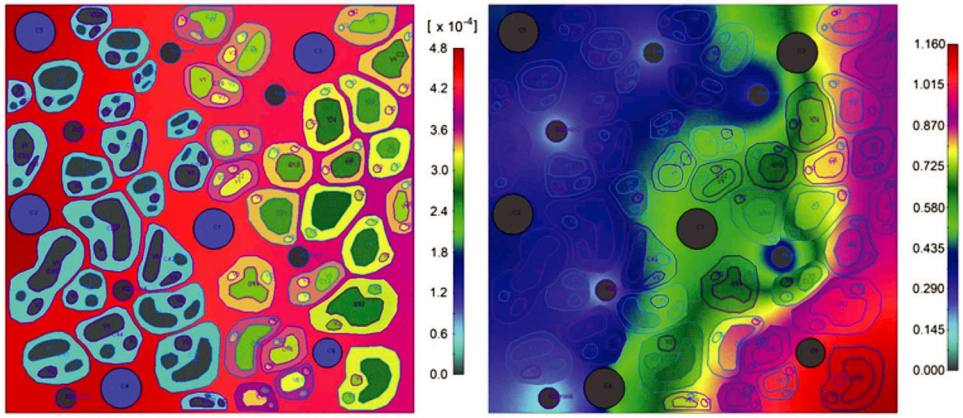

Fig. 16. Concentration (left panel) and electrical potential fields (right panel) at time t = 1s, coupled diffusion and electrical flow, detailed model.

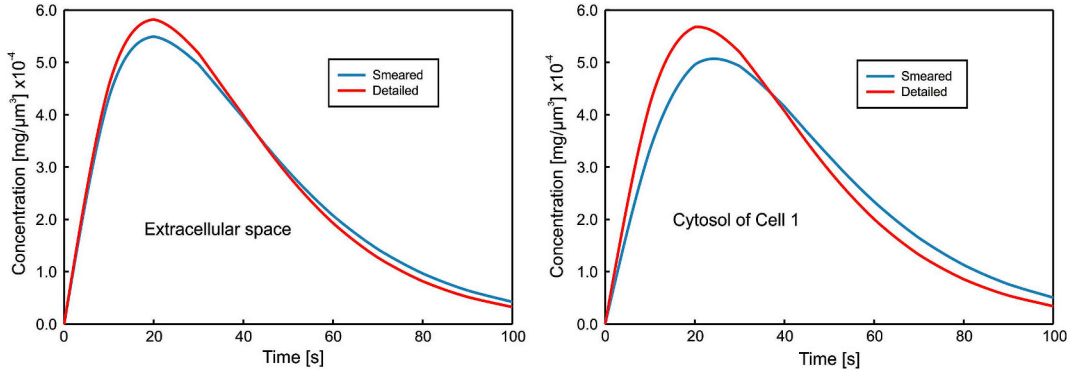

Fig. 17. Mean concentration vs. time for coupled problem, detailed and smeared model solutions, within extracellular space (left panel) and cytosol of cell type 1 (right panel).

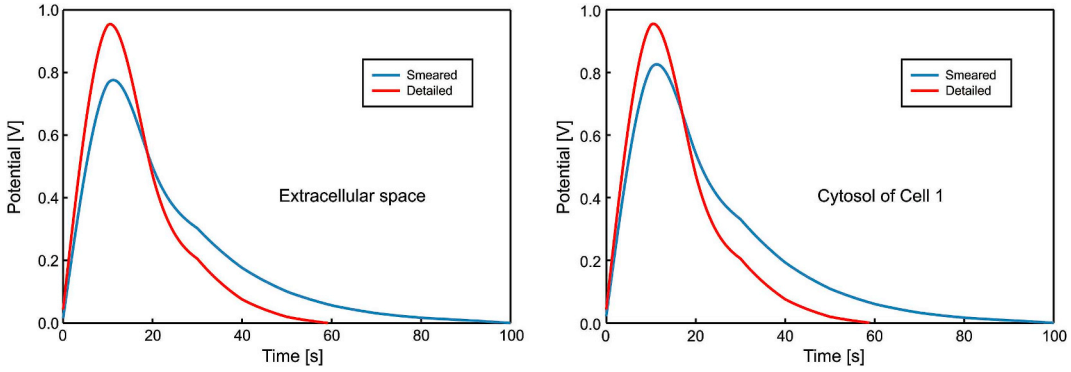

Fig. 18. Mean electrical potential vs. time for coupled problem, detailed and smeared model solutions, within extracellular space (left panel) and cytosol of cell type 1 (right panel).

(spatially fictitious) at nodes which take into account size and properties of membranes (walls) which physically separate the domains. Besides the good solution accuracy (in comparison with detailed models), the smeared models are easy to generate when simulating processes within complex structures and geometrical shapes of biological systems. Furthermore, the smeared models (implemented in our multipurpose software package PAK [33]) are orders of magnitude smaller in the number of equations when compared to detailed models. Thus, we conclude that presented FE models based on the smeared concept offer a novel computational tool for practical applications in biomedical investigations.

Acknowledgments

The authors acknowledge support from the City of Kragujevac, Serbia.

Appendix 1

FE model of electric conduction in nerves based on the cable theory, formulation of the composite cable finite element (CCFE)

We formulate a 1D finite element for electric conduction using the fundamental equation for electric conduction along fibers according to the so-called cable theory; this specific finite element is called Composite Cable Finite Element (CSFE). The theory was initiated William Thomson in 1850s who developed mathematical models of signal decay in telegraphic cables. Later, these models were implemented and experimentally verified in neuroscience.

Analytical solution. In accordance with equations (10) and (11), the cable equation in which both axial and lateral currents are taken into account, can be written as

$$G_a \frac{\partial^2 V_e^{in}}{\partial x^2} = G_m (V_e^{in} - V_e^{ext}) + C_m \left(\frac{\partial V_e^{in}}{\partial t} - \frac{\partial V_e^{ext}}{\partial t} \right) + I_{ion} \tag{A.1}$$

In order to compare numerical solution using our composite cable finite element (CCFE), we will omit the ionic current I_{ion} and assume that the external potential is V_e^{ext} is equal to zero. These assumptions do not reduce the proof of the validity and accuracy of the CCFE. Hence, the equation (A1) can be written as

$$\frac{1}{\eta} \frac{\partial^2 V_e^{in}}{\partial x^2} = c_m \frac{\partial V_e^{in}}{\partial t} + \frac{V_e^{in}}{r_m} \tag{A.3}$$

were r_m (Ω·mm) and c_m (F/mm) are membrane resistivity and capacitance, respectively, and η (in Ω/mm) is the longitudinal intracellular resistance per unit length; they can be expressed as

$$r_m = \frac{R_m}{2\pi r} = \frac{1}{2\pi r\, G_m} \tag{A.4}$$

$$c_m = C_m 2\pi r \tag{A.5}$$

$$r_l = \frac{\rho_l}{\pi r^2} = \frac{1}{G_a \pi r^2} \tag{A.6}$$

where G_m is specific membrane conductance (Siemens/mm^2), inverse of R_m; ρ_l (Ω·mm) is electrical resistance of the axoplasm; G_a is the nerve conductance (in Siemens/mm).

Further, a length constant λ can be introduced as a parameter that indicates how far a stationary current will influence the voltage along the cable. The length constant can be specified as

$$\lambda = \sqrt{\frac{r_m}{r_l}} \tag{A.7}$$

The first term at the right-hand side of (A3) affects the rate of change of the potential, which tends to a steady state distribution with time increase (theoretically – infinite time, practically – enough large time period). The steady state condition corresponds to $c_m = 0$, so that (A.3) reduces to

$$\lambda^2 \frac{d^2 V_e^{in}}{dx^2} = V_e^{in} \tag{A.8}$$

A general solution of this equation is

$$V_e^{in} = C_1 e^{x/\lambda} + C_2 e^{-x/\lambda} \tag{A.9}$$

Constants C_1 and C_2 can be determined from boundary conditions. We will further use the conditions as in our numerical solutions: x = 0, V = V_0; x = L, V_L = 0, where L is the length along the cable. Then, the solution is

$$V_e^{in} = \frac{V_0}{e^{L/\lambda} - e^{-L/\lambda}} \left(e^{\frac{L-x}{\lambda}} - e^{-\frac{L-x}{\lambda}} \right) \tag{A.10}$$

Composite Cable Finite element. A 1D finite element model for a nerve fiber is schematically shown in Fig. A1.

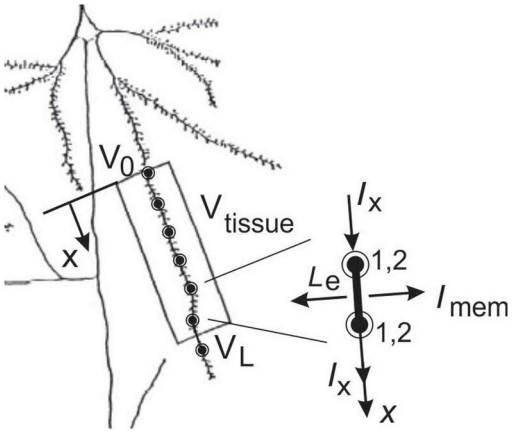

Fig. A1. Composite Cable Finite Element (CCFE). The element includes axial conduction along the element axis (current I_x) and lateral between the fiber and the surrounding tissue (current I_{mem}). The axial conduction is modeled by the 1D conductivity FE terms, while the lateral part is modeled by the connectivity elements 1,2 at each node.

The axial conduction balance equation, for the equilibrium iteration *i*, of the CCFE is represented in a standard form - equation (7), which, for the 2-node element with nodes *I* and *J*, is

$$K_{IJ}^a \Delta V_e^{inJ(i)} = I_I^{ext} - K_{IJ}^a V_e^{inJ(i-1)}, \quad I, J = 1,2; \ \ sum\ on\ J \tag{A.11}$$

where I_I^{ext} is the current coming from the neighboring elements (the I_I^{ext} cancel for all internal nodes of the FE system), and the matrix terms are

$$K_{11}^a = K_{22}^a = -K_{12}^a = -K_{21}^a = \frac{\pi r^2}{L_e} G_a \tag{A.12}$$

where L_e is the element length.

The lateral electric flow is modeled by connectivity elements 1,2. The connectivity element represents the electric flow through the surface belonging to the element. For a node *J* the size of this surface is

$$A_J = 2r\pi L_J \tag{A.13}$$

where L_J is the length belonging to the node. Then, the balance equation for the element 1,2 at the node *J* is

$$\left(\frac{1}{\Delta t} M_{IJ}^m + K_{IJ}^m \right) \Delta V_J^{(i)} = -\left(\frac{1}{\Delta t} M_{IJ}^m + K_{IJ}^m \right) V_J^{(i-1)} + \frac{1}{\Delta t} M_{IJ}^m V_J^t \tag{A.14}$$

where V_1 and V_2 are potentials in the fiber V_e^{in} and the surrounding tissue V_e^{ext}, respectively; V_J^t is potential at start of times step; and the matrices are

given by equation (13) where the surface area A_{mem} is evaluated according to (A.13).

Numerical results. The goal is to validate accuracy of the CCFE element by comparing numerical results with the analytical solution (A.10). Data used in numerical FE model are:

$V_0 = 1$ mV; $V_L = 0$; L = 10 mm (length of the domain), cable diameter r = 0.5 mm, Ranges of values used in numerical solutions are:

- G_a = [1, 100] [S/mm]
- G_m = [1, 100] [S/mm^2]
- c_m = [0, 1, 100] (F/mm^2)

FE model consists of 1D composite cable finite elements (CCFEs), and surrounding continuum with prescribed V = 0 at all nodes (Fig. A2). Dimension of the continuum is 10 × 1 mm, and FE division is 100 x 2. There are also 100 CCFEs.

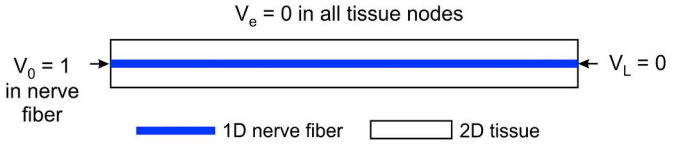

Fig. A2. FE model of nerve fiber (CCFE elements) with surrounding 2D tissue.

Distribution of electrical potential in 1D fiber, for three values of the nerve conductance G_a, is shown on Fig. A3. It can be seen how the electrical signal propagation increases with G_a.

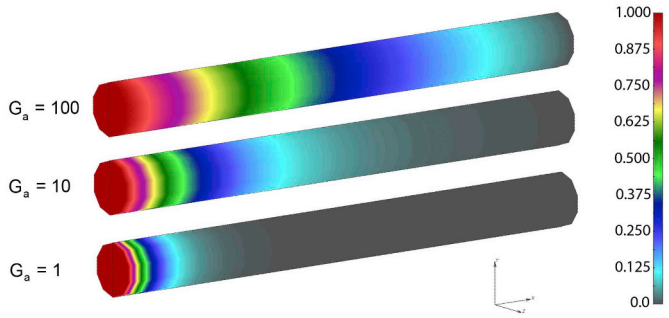

Fig. A3. Distribution of electrical potential in in the nerve fiber at stationary state, for case with: G_a = 1, 10, 100, and G_m = 1, c_m = 1.

We have selected several material data sets to illustrate how the material parameters affect the solutions. The data sets, and the values of length constant, λ, are:

G_a = 1, G_m = 1, r = 0.5, λ = 0.5

G_a = 100, G_m = 1, r = 0.5, λ = 7.07

G_a = 1, G_m = 100, r = 0.5, λ = 0.0707

G_a = 100, G_m = 100, r = 0.5, λ = 0.71

Diagrams of electric potential distribution along nerve fiber in the stationary state are shown in Fig. A4. There is evident agreement between the numerical and analytical solutions. It can be seen that solutions G_a = 1, G_m = 1 and G_a = 100, G_m = 100 are the same, while increase of G_m leads to decrease of the electrical propagation length.

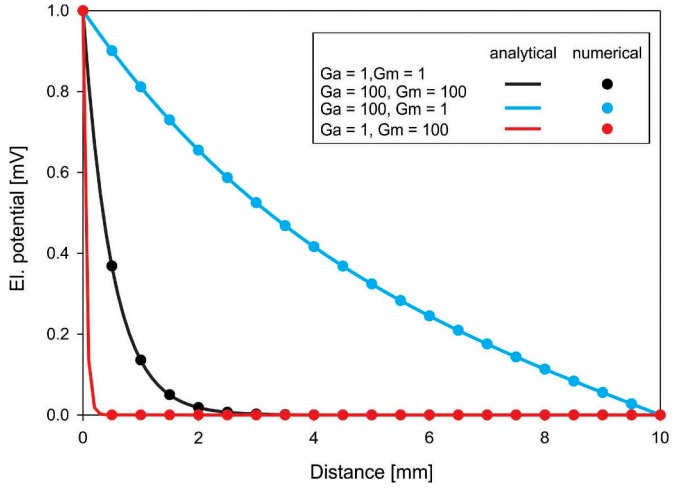

Fig. A4. Electrical potential vs. length of nerve (analytical and numerical solution) for stationary state for various (G_a, G_m) values, c_m = 1.

Change of the potential profiles over time, for G_a = 100, G_m = 1, c_m = 10, is shown in Fig. A5. It can be seen from this figure how the profiles

approach to the stationary shape. The stationary profile is reached after 20s, since after that time the profiles remain practically the same (changes of potential in all points become very small).

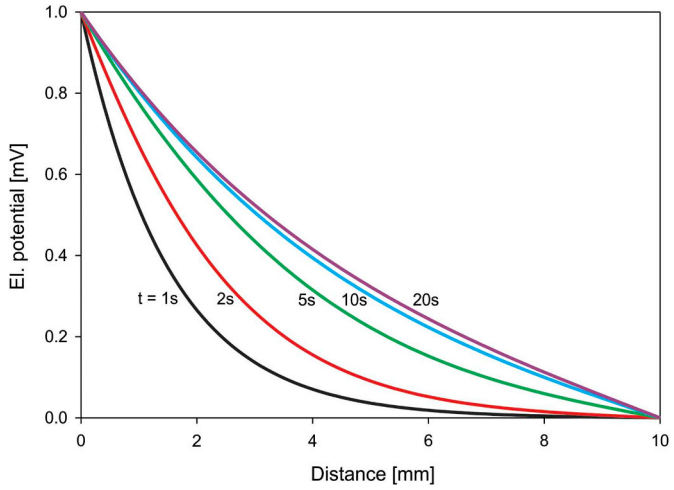

Fig. A5. Electrical potential profiles for several time moments during transient states. Data: $G_a = 100$, $G_m = 1$, $c_m = 10$. The stationary profile is reached at t = 20s.

Finally, we show in Fig. A6 how time for reaching the stationary state depends on the specific capacitance of membrane c_m. It can be seen that dependence is linear.

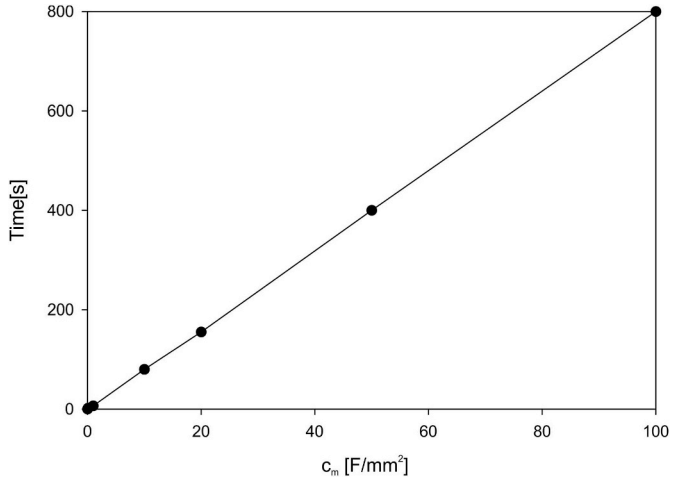

Fig. A6. Time of reaching the stationary state vs. specific capacitance of membrane (c_m), for $G_a = 1$, $G_m = 1$.

Appendix 2

Computation of the ionic currents through cell membranes

Here are presented the fundamental relations for calculation of membrane currents of potassium and sodium according to Ref. [2], and further implementation of these relations into the incremental-iterative FE form. These relations are experimentally determined for Purkinje fibers.

The potassium current I_K is expressed as (in μA/cm^2)

$$I_K = (g_{K1} + g_{K2})(V_m - V_K) \tag{A1}$$

where g_{K1} and g_{K2} are membrane conductivities, V_m (in mV) is the membrane potential (defined as the difference between potentials inside and outside of cell, and V_K is equilibrium potential (in Ref. [2] taken to be -100mV); dimension of g_{K1} and g_{K2} is [μA/(cm^2 mV)]. According to experimental measurements, the expressions for the conductivities are:

$$g_{K1} = 1.2\exp[(-V_m - 90)/50] + 0.015\exp[(V_m + 90)/60] \tag{A2}$$

$$g_{K2} = 1.2n^4$$

where

$$\frac{dn}{dt} = \alpha_n(1 - n) - \beta_n n \tag{A3}$$

where

$$\alpha_n = \frac{0.0001(-V_m - 50)}{\exp[(-V_m - 50)/10] - 1}, \quad \beta_n = 0.002\exp[(-V_m - 90)/80]$$

For sodium current density I_{Na} the expression is

$$I_{Na} = g_{Na}(V_m - V_{Na}) \tag{A4}$$

where $V_{Na} = 40$ mV and

$$g_{Na} = 400m^3h + 0.14 \tag{A5}$$

Expressions for parameters m and h are as follows:

$$\frac{dm}{dt} = \alpha_m(1 - m) - \beta_m m \tag{A6}$$

where

$$\alpha_m = \frac{0.1(-V_m - 48)}{\exp[(-V_m - 48)/15] - 1}, \quad \beta_m = \frac{0.12(V_m + 8)}{\exp[(V_m + 8)/5] - 1} \tag{A7}$$

and

$$\frac{dh}{dt} = \alpha_h(1 - h) - \beta_h h \tag{A8}$$

where

$$\alpha_h = 0.17\exp[(-V_m - 90)/20], \quad \beta_h = \left[\exp\left(\frac{-V_m - 42}{10}\right) + 1\right]^{-1} \tag{A9}$$

We further integrate equation (A3) and (A6) within time step. Equation (A3) can be written as

$$\frac{dn}{dt} = \alpha_n - (\alpha_n + \beta_n)n$$

Implicit integration scheme is used within time step Δt, so that

$$n^{t+\Delta t} = \frac{1}{(\alpha_n + \beta_n)}\{\alpha_n - [\alpha_n - (\alpha_n + \beta_n)n^t]\exp[-(\alpha_n + \beta_n)\Delta t]\} \tag{A10}$$

where the right-upper indices t and $t + \Delta t$ refer to the start and end of time step.

The analogous expression can be obtained for the parameters m and h:

$$m^{t+\Delta t} = \frac{1}{(\alpha_m + \beta_m)}\{\alpha_m - [\alpha_m - (\alpha_m + \beta_m)m^t]\exp[-(\alpha_m + \beta_m)\Delta t]\}$$

$$h^{t+\Delta t} = \frac{1}{(\alpha_h + \beta_h)}\{\alpha_h - [\alpha_h - (\alpha_h + \beta_h)h^t]\exp[-(\alpha_h + \beta_h)\Delta t]\} \tag{A11}$$

With these coefficients determined for the end of time step, the conduction coefficients can be determined and the currents specified in (A1) and (A4) can be calculated. We calculate coefficients in (A7) and (A9) using the corresponding mean values of membrane potential V_m,

$$V_m = \frac{1}{2}(V_m^t + V_m^{t+\Delta t}) \tag{A12}$$

Funding

This paper is supported by the SILICOFCM project that has received funding from the European Union's Horizon 2020 research and innovation programme under grant agreement No 777204. This article reflects only the author's view. The Commission is not responsible for any use that may be made of the information it contains. This research was also funded by Ministry of Education and Science of Serbia, grants OI 174028 and III 41007.

Conflict of interest statement

There is no Conflict of Interest.

References

[1] A.L. Hodkin, A.F. Huxley, A quantitative description of membrane current and its application to conduction and excitation in nerve, J. Physiol. 117 (1952) 500–544.
[2] D. Noble, A modification of the Hodgkin-Huxley equations applicable to Purkinje fibre action and pace-maker potentials, J. Physiol. 160 (1962) 317–352.
[3] S.M. Baer, J. Rinzel, Propagation of dendritic spikes mediated by excitable spines: a continuum theory, J. Neurophysiol. 65 (1991) 874–890.
[4] K.F. Decker, J. Heijman, J.R. Silva, T.J. Hund, Y. Rudy, Properties and ionic mechanisms of action potential adaptation, restitution, and accommodation in canine epicardium, Am. J. Physiol. Heart Circ. Physiol. 296 (2009) H1017–H1026.
[5] T. O'Hara, L. Virág, A. Varró, Y. Rudy, Simulation of the undiseased human cardiac ventricular action potential: model formulation and experimental validation, PLoS Comput. Biol. 7 (2011) e1002061-e1002090.
[6] T. Ijiri, T. Ashihara, T. Yamaguchi, e.a. K. Takayama, A procedural method for modeling the Purkinje fibers of the heart, J. Physiol. Sci. 58 (2008) 481–486.
[7] J.E. Hall, Guyton and Hall Textbook of Medical Physiology, 13 ed., Elsevier, 2016.
[8] W.F. Born, E.L. Boulpaep, Medical Physiology, Updated Edition, Elsevier Saunders, Philadelphia, 2005.
[9] J. Keener, J. Sneyd, Mathematical Physiology I: Cellular Physiology, II: Systems Physiology, 2 ed., Springer, 2009.

[10] R.L. Winslow, Theoretical foundations of neural modeling, BME 580.681, The John Hopkins Univ. Sch, Medicine and Whiting Sch Engrg, Baltimore, 1992.
[11] R.H. Clayton, A.V. Panfilov, A guide to modelling cardiac electrical activity in anatomically detailed ventricles, Prog. Bioph. Mol. Biol. 96 (96) (2008) 19–43.
[12] P. Lafortune, R. Arís, M. Vázquez, G. Houzeaux, Coupled electromechanical model of the heart: parallel finite element formulation, Int. J. Numer. Meth. Biomed. Eng. 28 (2012) 72–86.
[13] H. Dal, S. Göktepe, M. Kaliske, E. Kuhl, A fully implicit finite element method for bidomain models of cardiac electromechanics, Comput. Methods Appl. Mech. Eng. 253 (2013) 323–336.
[14] B.M. Rocha, F. Kickinger, A.J. Prassl, G. Haase, E.J. Vigmond, R.W.d. Santos, S. Zaglmayr, G. Plank, A macro finite element formulation for cardiac electrophysiology simulations using hybrid unstructured grids, IEEE Trans. Biomed. Eng. 58 (2011) 1055–1065.
[15] M. Kojic, M. Milosevic, N. Kojic, E.J. Koay, J.B. Fleming, M. Ferrari, A. Ziemys, Extension of the composite smeared finite element (CSFE) to include lymphatic system in modeling mass transport in capillary systems and biological tissue, J. Serb. Soc. Comp. Mech. 11 (2017) 108–120.
[16] M. Milosevic, V. Simic, B. Milicevic, E.J. Koay, M. Ferrari, A. Ziemys, M. Kojic, Correction function for accuracy improvement of the Composite Smeared Finite Element for diffusive transport in biological tissue systems, Comp. Meth. Appl. Mech. Eng. (2018), https://doi.org/10.1016/j.cma.2018.1004.1012.
[17] M. Kojic, M. Milosevic, V. Simic, E.J. Koay, N. Kojic, A. Ziemys, M. Ferrari, Multiscale smeared finite element model for mass transport in biological tissue: from blood vessels to cells and cellular organelles, Comput. Biol. Med. 99 (2018) 7–23.
[18] M. Kojic, M. Milosevic, V. Simic, E.J. Koay, J.B. Fleming, S. Nizzero, N. Kojic, A. Ziemys, M. Ferrari, A composite smeared finite element for mass transport in capillary systems and biological tissue, Comp. Meth. Appl. Mech. Eng. 324 (2017) 413–437.
[19] M. Kojic, Smeared concept as a general methodology in finite element modeling of physical fields and mechanical problems in composite media, J. Serb. Soc. Comp. Mech. 12 (2) (2018) 1–16.
[20] N. Kim, M.B. Cannell, P.J. Hunter, Changes in the calcium current among different transmural regions contributes to action potential heterogeneity in rat heart, Prog. Biophys. Mol. Biol. 103 (2010) 28–34.
[21] P.J. Hunter, A.D. McCulloch, H.E.D.J.t. Keurs, Modelling the mechanical properties of cardiac muscle, Prog. Biophys. Mol. Biol. 69 (1998) 289–331.
[22] A. Santiago, Fluid-Electro-Mechanical Model of the Human Heart for Supercomputers, Universitat Politècnica de Catalunya, Bacelona, 2018.
[23] S.M. Mijailovich, B. Stojanovic, M. Kojic, A. Liang, V.J. Wedeen, R.J. Gilbert, Derivation of a finite-element model of lingual deformation during swallowing from the mechanics of mesoscale myofiber tracts obtained by MRI, J. Appl. Physiol. 109 (2010) 1500–1514.
[24] J. Schaff, C.C. Fink, B. Slepohenko, J.H. Carson, L.M. Loew, A general computational framework for modeling cellular structure and function, Biophys. J. 73 (1997) 1135–1146.
[25] S. Trapp, R.W. Horobin, A predictive model for the selective accumulation of chemicals in tumor cells, Eur. Biophys. J. 34 (2005) 959–966.
[26] M. Kojic, N. Filipovic, B. Stojanovic, N. Kojic, Computer Modeling in Bioengineering - Theoretical Background, Examples and Software, John Wiley and Sons, Chichester, England, 2008.
[27] M. Kojic, N. Filipovic, B. Stojanovic, N. Kojic, Computer Modelling in Bioengineering – Theory, Examples and Software, John Wiley and Sons, Chichester, 2008.
[28] K.J. Bathe, Finite Element Procedures, Prentice Hall, Upper Sadle River, N.J., 1996.
[29] M. Kojic, K.J. Bathe, Inelastic Analysis of Solids and Structures, Springer, Berlin,Heidelberg, New York, 2005.
[30] M. Milosevic, D. Stojanovic, V. Simic, B. Milicevic, A. Radisavljevic, P. Uskokovic, M. Kojic, A computational model for drug release from PLGA implant, Materials 11 (2018) 2416 https://doi.org/2410.3390/ma11122416.
[31] P.M. Boyle, M. Deo, E.J. Vigmond, Behaviour of the purkinje system during defibrillation-strength shocks, Proc. 29th Annual International Conference of the IEEE EMBS Cité Internationale, IEEE, Lyon, 2007, pp. 419–422.
[32] X. Zhang, K. Shedden, G.R. Rosania, A cell-based molecular transport simulator for pharmacokinetic prediction and cheminformatic exploration, Mol. Pharm. 3 (2006) 704–716.
[33] M. Kojic, R. Slavkovic, M. Zivkovic, N. Grujovic, N. Filipovic, M. Milosevic, PAK - Finite Element Program for Linear and Nonlinear Analysis, Univ Kragujevac and R& D Center for Bioengineering, Kragujevac, Serbia, 2010.
[34] R.H. Clayton, O. Bernus, E.M. Cherry, H. Dierckx, F.H. Fenton, L. Mirabella, A.V. Panfilov, F.B. Sachse, G. Seemann, H. Zhang, Models of cardiac tissue electrophysiology: progress,challenges and open questions, Prog. Biophys. Mol. Biol. 104 (2011) 22–48.
[35] J. Cooper, A. Corrias, D. Gavaghan, D. Noble, Considerations for the use of cellular electrophysiology models within cardiac tissue simulations, Prog. Biophys. Mol. Biol. 107 (2011) 74–80.
[36] M.O. Bernabeu, R. Bordas, P. Pathmanathan, J. Pitt-Francis, J. Cooper, A. Garny, D.J. Gavaghan, B. Rodriguez, J.A. Southern, J.P. Whiteley, CHASTE: incorporating a novel multi-scale spatial and temporal algorithm into a large-scale open source library, Phil. Trans. R. Soc. A 367 (2009) 1907–1930.
[37] B.J. Roth, J.J.P. Wikswo, A bidomain model for the extracellular potential and magnetic field of cardiac tissue, IEEE Trans. Biomed. Eng. 33 (1986) 467–469.
[38] C.S. Henriquez, Simulating the electrical behavior of cardiac tissue using the bidomain model, Crit. Rev. Biomed. Eng. 21 (1993) 1–77.
[39] C.S. Henriques, A.L. Muzikant, C.K. Smoak, Anisotropy, fiber curvature, and bath loading effects on activation in thin and thick cardiac tissue preparations: simulations in a three-dimensional bidomain model, J. Cardiov. Electrophysiol. 7 (1996) 424–444.
[40] J.P. Keener, A.V. Panfilov, A biophysical modelfor defibrillation of cardiac tissue, Biophys. J. 71 (1996) 1335–1345.
[41] A. Corrias, P. Pathmanathan, D.J. Gavaghan, M.L. Buista, Modelling tissue electrophysiology with multiple cell types: applications of the extended bidomain framework, Integr. Biol. 4 (2012) 192–201.
[42] M. Kojic, M. Milosevic, N. Kojic, K. Kim, M. Ferrari, A. Ziemys, A multiscale MD–FE model of diffusion in composite media with internal surface interaction based on numerical homogenization procedure, Comput. Methods Appl. Mech. Eng. 269 (2014) 123–138.
[43] E.J. Vigmond, B.D. Stuyvers, Modeling our understanding of the His-Purkinje system, Prog. Biophys. Mol. Biol. 120 (2016) 179–188.
[44] R.M. Bordas, K. Gillow, D. Gavaghan, B. Rodriguez, D. Kay, A bidomain model of the ventricular specialized conduction system of the heart, SIAM J. Appl. Math. 72 (2012) 1618–1643.
[45] D. Bruce, P. Pathmanathan, J.P. Whiteley, Modelling the effect of gap junctions on tissue-level cardiac electrophysiology, Bull. Math. Biol. 76 (2014) 431–454.
[46] Y. Cheng, Z. Yu, M. Hoshijima, M.J. Holst, A.D. McCulloch, J.A. McCammon, A.P. Michailova, Numerical analysis of Ca2+ signaling in rat ventricular myocytes with realistic transverse-axial tubular geometry and inhibited sarcoplasmic reticulum, PLoS Comput. Biol. 6 (2010) e1000972-1000992.
[47] Z. Yu, G. Yao, M. Hoshijima, A. Michailova, M. Holst, Multiscale modeling of calcium dynamics in ventricular myocytes with realistic transverse tubules, IEEE Trans. Biomed. Eng. 58 (2011) 2947–2951.
[48] M.A. Walker, G.S.B. Williams, T. Kohl, S.E. Lehnart, M.S. Jafri, J.L. Greenstein, W.J. Lederer, R.L. Winslow, Superresolution modeling of calcium release in the heart, Bioph. J. 107 (2014) 3018–3029.
[49] P.M. Kekenes-Huskey, Y. Cheng, J.E. Hake, F.B. Sachse, J.H. Bridge, M.J. Holst, A. McCammon, A.D. McCulloch, A.P. Michailova, Modeling effects of L-type Ca^{2+} current and Na^{+}-Ca^{2+} exchanger on Ca^{2+} trigger flux in rabbit myocytes with realistic t-tubule geometries, Comp. Phys. Med. 3 (2012) 1–14.
[50] J. Schaff, C.C. Fink, B. Slepohenko, J.H. Carson, L.M. Loew, A general computational framework for modeling cellular structure and function, Biophys. J. 73 (1997) 1135–1146.
[51] E.M. Cherry, H.S. Greenside, C.S. Henriquez, Efficient simulation of three-dimensional anisotropic cardiac tissue using an adaptive mesh refinement method, Chaos 13 (2003) 853–865.
[52] E.J. Vigmond, F. Aguel, N.A. Trayanova, Computational techniques for solving the bidomain equations in three dimensions, IEEE Trans. Biomed. Eng. 49 (2002) 1260–1269.
[53] P. Pathmanathan, M.O. Bernabeu, R. Bordas, J. Cooper, A. Garny, J.M. Pitt-Francis, J.P. Whiteley, D.J. Gavaghan, A numerical guide to the solution of the bidomain equations of cardiac electrophysiology, Prog. Biophys. Mol. Biol. 102 (2010) 136–155.
[54] J.P. Whiteley, An efficient numerical technique for the solution of the monodomain and bidomain equations, IEEE Trans. Biomed. Eng. 53 (2006) 2139–2147.
[55] E.J. Vigmond, R.W.d. Santos, A.J. Prassl, M. Deo, G. Plank, Solvers for the cardiac bidomain equations, Prog. Biophys. Mol. Biol. 96 (2008) 3–18.
[56] C.R. Xavier, R.S. Oliveira, V.F. Vieira, R.W.d. Santos, W.M. Jr, Multi-level parallelism for the cardiac bidomain equations, Int. J. Parallel. Prog. 37 (2009) 572–592.
[57] J.P. Whiteley, Physiology driven adaptivity for the numerical solution of the bidomain equations, Ann. Biomed. Eng. 35 (2007) 1510–1520.
[58] R. Bordas, B. Carpentieri, G. Fotia, F. Maggio, R. Nobes, J. Pitt-Francis, J. Southern, Simulation of cardiac electrophysiology on next-generation high-performance computers, Phil. Trans. R. Soc. A 367 (2009) 1951–1969.
[59] J.A. Southern, G. Plank, E.J. Vigmond, J.P. Whiteley, Solving the coupled system improves computational efficiency of the bidomain equations, IEEE Trans. Biomed. Eng. 56 (2009) 2404–2412.
[60] Z. Qu, G. Hub, A. Garfinkel, J.N. Weiss, Nonlinear and stochastic dynamics in the heart, Phys. Rep. 543 (2014) 61–162.
[61] H. Dal, S. Göktepe, M. Kaliske, E. Kuhl, A fully implicit finite element method for bidomain models of cardiac electromechanics, Comput. Methods Appl. Mech. Eng. 253 (2013) 323–336.
[62] E. Berberoglu, H.O. Solmaz, S. Göktepe, Computational modeling of coupled cardiac electromechanics incorporating cardiac dysfunctions, Eur. J. Mech. Solids 48 (2014) 60–73.
[63] M. Kojic, M. Milosevic, V. Simic, B. Milicevic, V. Geroski, S. Nizzero, A. Ziemys, N. Filipovic, M. Ferrari, Smeared Multiscale Finite Element Models for Mass Transport and Electrophysiology Coupled to Muscle Mechanics, (2019) (submitted for publication).
[64] S. Mijailovich, O. Kayser-Herold, B. Stojanovic, D. Nedic, T. Irving, M. Geeves, Three-dimensional stochastic model of actin–myosin binding in the sarcomere lattice, J. General Physiol. 148 (2016) 459–488.
[65] P. Pathmanathan, R.A. Gray, Validation and trustworthiness of multiscale models of cardiac electrophysiology, Front. Physiol. 9 (2018), https://doi.org/10.3389/fphys.2018.00106.
[66] R.A. Gray, P. Pathmanathan, Patient-specific cardiovascular computational modeling: diversity of personalization and challenges, J. Cardiov. Translat. Res. 11 (2018) 80–88.
[67] P. Pathmanathan, G.R. Mirams, J. Southern, J.P. Whiteley, The significant effect of the choice of ionic current integration method in cardiac electro-physiological simulations, Int. J. Numer. Meth. Biomed. Eng. 27 (2011) 1751–1770.